# Elasticity of dense anisotropic carbons: A machine learning model of the structure–property relationship informed by large scale molecular dynamics data

Franck Polewczyk, Jean-Marc Leyssale, Philippe Aurel, Nicolas Pineau, Christophe Denoual, Gerard Vignoles, Paul Lafourcade

# Elasticity of dense anisotropic carbons: a machine learning model of the structure-property relationship informed by large scale molecular dynamics data

Franck Polewczyk[a,b,c], Jean-Marc Leyssale[c,*], Philippe Aurel[c], Nicolas Pineau[a,b], Christophe Denoual[a,b], Gerard L. Vignoles[d], Paul Lafourcade[a,b,*]

[a] *CEA DAM DIF, 91297 Arpajon, France*
[b] *University of Paris-Saclay, LMCE, 91680 Bruyères-le-Châtel, France*
[c] *University of Bordeaux, CNRS, Bordeaux INP, ISM, UMR 5255, F-33400 Talence, France*
[d] *University of Bordeaux, CNRS, CEA, Safran: LCTS (UMR5801), F-33600 Pessac, France*

**Abstract**

Dense anisotropic carbons are praised materials for thermostructural applications, yet, so far, a detailed structure-property relationship for these materials is still lacking, especially for the pyrocarbon (pyC) matrices in carbon/carbon composites. Here we compute the full elastic tensors of 210 recently introduced nanoscale models of anisotropic carbons [Polewczyk et al. Carbon 212 (2023) 118109], covering domain sizes ($L_c$ and $L_a$) and orientation angles (OA, as a measure of nanotexture) relevant to most as-prepared and moderately heat-treated pyC matrices: $L_c \in$ [1.5:8 nm]; $L_a \in$ [2:5.5 nm]; and OA $\in$ [25:110°]. Isothermal and adiabatic elastic tensors, corresponding to the slow quasi-static and ultra-fast loading regimes, respectively, are considered. Analysing the database of computed elastic constants with a random forest regressor supervised learning algorithm we show that all elastic constants can be predicted accurately using $L_c$, $L_a$ and OA as descriptors. Among the latter, OA is the one showing, by far, the strongest correlation with the elastic tensors. For such dense, non porous carbons, 3 of the 6 isothermal and 5 of the 6 adiabatic constants can even be accurately predicted using OA as the unique material descriptor. Calculation of the universal anisotropy index shows that isothermal tensors show more anisotropy than adiabatic ones, indicating that stress relaxation favors elastic anisotropy. Eventually, the Young's moduli and Poisson coefficients of six models of actual pyCs are presented and their longitudinal moduli compared to tensile measurements, showing relatively poor agreement. These results suggest that accounting for texture at a larger scale is required to capture pyC matrices elasticity. The developed supervised learning model is available for online use at `https://web.ism.u-bordeaux.fr/rfr`.

## 1. Introduction

Combining low weight and a high melting point [1], as well as a high displacement threshold energy [2], dense anisotropic carbons are key constituents in numerous cutting-edge materials for applications under extreme environments such as high temperature, high heat flux, high stress, or high-energy particle fluxes conditions. The most common example of such materials are certainly the so-called carbon fiber reinforced carbon matrix composites, or C/C composites [3, 4], finding numerous applications [5] in the fields of aerospace [6, 7] and aeronautics [8].

These materials are generally manufactured by deposition of a pyrolytic carbon (pyC) on the inner surfaces of a porous carbon fiber fabric, via the chemical vapor infiltration (CVI) technique[9, 10, 11]. Both the fibers and pyC matrices are dense carbons with a varying degree of anisotropy, also referred to as "texture", that correspond to a preferential orientation of the graphene layers within the materials. The anisotropy of the constituents confers them some important mechanical and thermal anisotropy, allowing to fine tune the composite materials to some prescribed mechanical and thermal properties.

Aside from C/C composites, pyCs are also found as interphases in C/SiC materials [12, 13] for the same types of applications [14] or as interphases in SiC/SiC ceramic matrix composites for GenIV nuclear reactors or nuclear fusion reactors [15, 16, 17] or as nuclear fuel cell coatings in the tristructural isotropic (TRISO) particles of the high temperature reactor (HTR) technology [18]. They are also considered as electrode materials [19]. Finally, thanks to their excellent hemocompatibility, they are used in medical implants and devices [20].

Common to pyC matrices and C fibers is the limited extent of the "crystalline" order within these graphene-based materials and the turbostratic (i.e. disordered) stacking of those layers in the 002 direction. With densities in the 1.9-2.2 g/cm$^3$ range [21, 22], pyC matrices contain very little

*Corresponding author
*Email addresses:* `jean-marc.leyssale@u-bordeaux.fr` (Jean-Marc Leyssale), `paul.lafourcade@cea.fr` (Paul Lafourcade)

to no porosity. C fibers are generally slightly less dense (i.e. $\sim 1.8$ g/m$^3$ for PAN-based fibers [23]), yet they can still be considered as dense carbons. At the sub-micrometer scale (or a few tens of nm), the structure of the pyC matrices can be described by a few observables extracted from diffraction experiments. The $L_c$ and $L_a$ lengths, extracted from the width of the 002 peak and 10 asymmetric band in X-ray (or neutron) diffraction patterns characterize the extent of coherent domains in the out-of-plane and in-plane directions, respectively, and the position of the 002 peak allows extracting the inter-layer distance $d_{002}$, generally slightly larger, by $\sim 0.1$ Å, than for crystalline graphite.

Another important parameter in characterizing the texture (or nanotexture) of these materials at the nanoscale is the so-called orientation angle (OA), defined as the full width at half maximum of the angular intensity profile of the 002 arcs in selected area electron diffraction (SAED) patterns [24]. As such, OA measures the distribution of the 002 direction with respect to the deposition direction (fiber surface) and is thus an excellent measure of the anisotropy at this scale. Several authors have proposed some nanotexture classifications of pyCs based on OA values [24, 25]. Following Reznik and Hüttinger [25], pyCs with OA = 180°, $180° > OA \geq 80°$, $80° > OA \geq 50°$ and $OA < 50°$ are defined as isotropic (ISO), low texture (LT), medium texture (MT) and high texture (HT) pyCs, respectively. According to this classification, the long-known rough laminar (RL) and smooth laminar (SL) pyrocarbons belong to the HT and MT categories, respectively. Although these concepts also apply to fibers, the axial symmetry of the latter slightly complicates the situation. Especially, the contributions of in-plane order along, and normal to, the fiber axis have to be distinguished with two independent $L_a$ values [26].

While measurements of the full elastic tensors of carbon fibers are frequently reported in the literature [27, 28, 29], very limited data exist for the pyC matrices due to the difficulty of measurements for such materials that are generally obtained as thin deposits on complex substrates (*i.e.* fibrous preforms). To our knowledge, only two sets of values have been reported for HT pyCs [30, 31], based on ultrasonic measurements. Noticeably, the values reported for the in-plane elastic constant $C_{11}$, 40-50 GPa, and the corresponding Young's modulus $E_1$, 27-39 GPa, are more than an order of magnitude lower than the values for graphite, 1060 and 1020 GPa for $C_{11}$ and $E_1$, respectively [32]. In order to rationalize these findings, Böhlke *et al.* [33] and Lin *et al.* [34] have proposed micromechanical models based on the extraction of graphene planes and local domains – the so called coherent domains – orientations from HRTEM images. Although promising, the obtained effective elastic constants remain considerably larger than those reported from ultrasonic measurements, close to one order of magnitude for $C_{11}$.

Tensile tests performed by Sauder *et al.* [35] using single compliant fibers coated by thin pyC deposits (*i.e.* microcomposites) have allowed extracting the in-plane moduli of various pyC textures, both as prepared and after several heat treatments. It was found that the SL pyC (MT) has a Young's modulus $E_1$ = 54 GPa, that does not change, even after heat treatments as high as 2200°C. $E_1$ for the RL pyC (HT) was found to be of 115 GPa, slightly decreasing to 95 GPa after heat treatment at 2200°C, which is slightly counter-intuitive. Far more counter-intuitive were the results obtained for the regenerative laminar (ReL) pyC, another HT pyC with similar anisotropy and domain sizes to the RL pyC. Although similar results to those for the RL pyC should have been expected, a much larger $E_1$ value, 205 GPa, was found for this pyC as prepared, and this value increased to 245 GPa and above 360 GPa after heat treatments at 1600 and 2200°C, respectively.

Also, because of its convenience to investigate the mechanical properties of coatings, pyC matrices were also subject to numerous indentation/nano-indentation tests [36, 37, 28, 38], yet it is now agreed that the indentation moduli are significantly affected by elastic instabilities, such as buckling, when the tests are performed in the parallel direction to the layers, such that it is not possible to recover the elastic constants or Young's modulus from these experiments [36, 39, 38].

Modelling the relationship between the structure, the texture and resulting elastic properties has proved to be a real challenge that only a few studies have explored [40, 41, 42, 43, 44]. Using the Image Guided Atomistic Reconstruction approach (IGAR) [45, 46], Farbos *et al.* have proposed several structural models of high texture pyCs at the nanoscale, including some as-prepared RL and ReL pyCs, as well as some ReL pyCs after various heat treatments [22]. The full elastic tensors were then computed [40], unraveling interesting structure-property relationships like, for instance, the effect of interlayer crosslinks on interlayer shear ($C_{44}$), yet the computed in-plane modulus $E_1$, of the order of 600 GPa, for all materials, is quite significantly larger than the above discussed experimental reports by Sauder *et al.* [35].

However, the IGAR models did not allow for a full investigation of the structure-elasticity relationship at the nanoscale. First, although very successful in capturing in-plane order (like the $L_a$ parameter), the obtained models were suffering from a strong underestimation of the out-of-plane coherence ($L_c$), and from a significant overestimation of the interlayer distance $d_{002}$. Moreover, by construction, only high texture pyCs can be modelled with this technique, and only a handful of IGAR models have been produced due to the requirement of having at hand a complete characterization database including density measurement, hydrogen-content and high quality high resolution transmission electron microscopy (HRTEM) images. Further, as structural and (nano-) textural properties are often correlated in actual pyCs (*i.e.* anisotropy, $L_a$ and $L_c$), it is difficult to disentangle

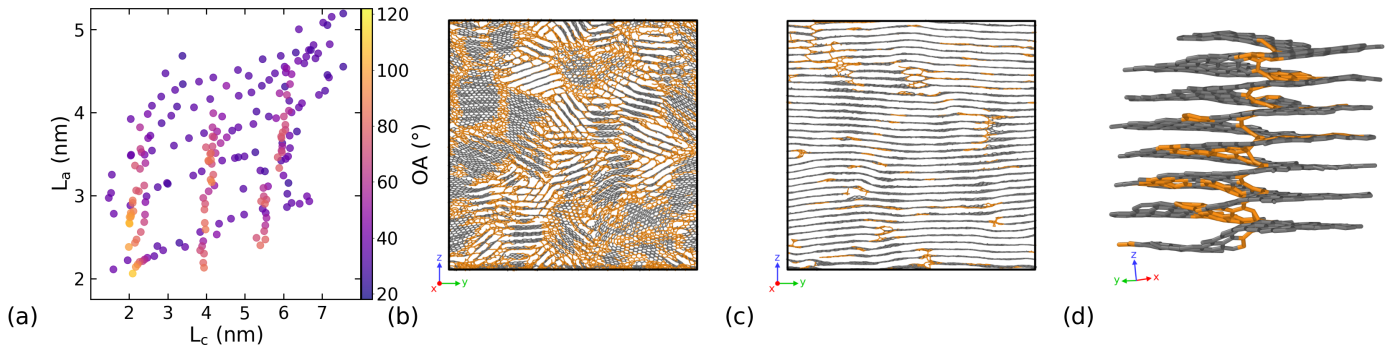


Figure 1: Overview of the synthetic microstructures database. (a) Distribution of models with $L_a$ as a function of $L_c$, colored by OA. 1 nm thick slices of (b) a LT model with $L_a$ = 2.8 nm, $L_c$ = 2 nm and OA = 94° and (c) a HT model with $L_a$ = 5.3 nm, $L_c$ = 7.7 nm and OA = 25°. (d) close view of a screw dislocation in the HT model from (c). Colors assigned to atoms in (a)–(c) correspond to hexagonal like environments (gray) and defects (orange).

the effects of structure and texture in a structure-property relationship.

In a recent work, Polewczyk *et al.* have proposed a polygranular variant of the IGAR method: the PG-IGAR method, in which atomistic models of dense textured carbons are produced from a limited set of structural and textural parameters [47]. A large database of models, covering both MT and HT pyCs have been produced, spanning wide – and uncorrelated – ranges of $L_a$, $L_c$ and OA values. In this report, we first attempt to propose a machine-learning derived structure-elasticity relationship based on the calculation of the full elastic tensors for all these models, both in the limits of high and low strain rates. Then, models identified to experimental actual pyCs, namely smooth laminar (SL), rough laminar (RL), regenerative laminar (ReL) as well as heat-treated ReL, are compared to their experimental counterparts.

## 2. Models and Methods

### *2.1. Database of atomistic models*

We recall here the principles of the PG-IGAR method and present briefly the model database. All the details can be found in Ref. 47. The basic idea behind PG-IGAR is to construct models from simple parameters that can be derived from X-Ray diffraction (XRD) and SAED patterns. The first step is the construction of 3D periodic cells with grains of average size $L_t$, related to $L_a$ and $L_c$ parameters, using the Voronoï tessellation technique. Then each grain is decorated with HRTEM-like straight fringes with periodicity given by the target $d_{002}$ and a statistical distribution of the 002 directions derived from a target $OA_t$ value. The obtained 3D image is then converted into an external potential and the cell filled in with carbon in the liquid state at the target density. The latter is then cooled down to room temperature using molecular dynamics, under the influence of a combination of the second-generation reactive empirical bond order potential (REBO2) [48] and an external 3D-image potential, according to a non-linear quenching scheme with duration $\tau_Q$, and finally relaxed at 300 K and 1 bar after removal of the image potential. Varying three of the simulation parameters, $L_t$, $OA_t$ and $\tau_Q$, the liquid carbon density and the textured image $d_{002}$ being fixed to 2.16 g/cm$^3$ and 0.345 nm, respectively, 210 models were obtained.

All the models, each containing a total of 206950 atoms enclosed in nearly cubic periodic cells of side lengths $\sim$ 12.4 nm, have been thoroughly analysed[47]. The distributions of local atomic environments (LAE) were computed as in Refs 49 and 2, as well as the size statistics of sp$^2$ bonded rings. The pair distribution functions $G(r)$ were also computed and converted by Fourier transform into structure factors $S(Q)$, from which values of $L_a$ and $L_c$ and $d_{002}$ were extracted. HRTEM images, simulated using Dr Probe software [50], were also converted into diffraction patterns by Fourier transform and the 002 arcs intensities analysed using an in-house script to extract OAs.

The database is graphically presented in figure 1. As shown in figure 1(a), it covers relatively scattered and uncorrelated values of $L_c$ and $L_a$ ranging from $\sim$ 1.5 to 7.5 nm and 2 to 5.5 nm, respectively, while OA values, ranging from 25 to 110°, covers characteristic values from HT to early LT carbons. Further, figure 1(a) also shows that OA values are mostly uncorrelated to $L_c$ and $L_a$, even though, amongst the database, the largest OAs correspond to rather small $L_a$ and $L_c$. The distribution of data points in the 3D ($L_a$, $L_c$, OA) space is not perfectly uniform, as these three parameters actually are outputs in the PG-IGAR simulations, and their precise values depends in a complex way of the simulations inputs (grain size, orientation distribution, interfringe spacing, atomic density and quench rate). Nevertheless, we assume here that the data points sampling is sufficient for the purpose of the present work.

Snapshots of LT and HT models, given in figures 1(b) and

1(c), respectively, highlight the fundamental difference between those microstructures. While the LT microstructure shows marked coherent domains, with distinct grain orientations and neat grain boundaries, the HT microstructure almost appears as a well oriented anisotropic structure with localized defects, even though some appear quite extended, such as the screw dislocation shown in a close-up in figure 1(d). Finally, it is worth mentioning that the three adopted descriptors of the structure and nanotexture of the models, namely $L_a$, $L_c$ and OA were correlated in Ref. 47 to the distributions of local environments and ring statistics using a machine-learning algorithm.

### *2.2. Elastic constants calculations*

Considering that the cartesian axis system is chosen so that the $z$ axis correspond to the direction of anisotropy (*i.e.* the center of the distribution of the 002 directions), and assuming transverse isotropic symmetry, the second-order elastic tensor in the Voigt contraction convention reads:

$$\boldsymbol{C} = \begin{pmatrix} C_{11} & C_{12} & C_{13} & 0 & 0 & 0 \\ C_{12} & C_{11} & C_{13} & 0 & 0 & 0 \\ C_{13} & C_{13} & C_{33} & 0 & 0 & 0 \\ 0 & 0 & 0 & C_{44} & 0 & 0 \\ 0 & 0 & 0 & 0 & C_{44} & 0 \\ 0 & 0 & 0 & 0 & 0 & C_{66} \end{pmatrix} \quad (1)$$

with 5 independent elastic constants as $C_{66} = (C_{11} - C_{12})/2$. In this equation, indices $1, 2$ and $3$ correspond to $x$, $y$, and $z$ axes respectively, index 4 corresponds to shear in the $xz$ or $yz$ planes, and index 6 to shear in the $xy$ plane.

In this work, these constants are computed using molecular dynamics (MD) simulations performed with the STAMP [51] (Simulations Temporelles Atomistiques Massivement Parallélisées) code along with the LCBOPII potential [52, 53]. MD trajectories are integrated using a velocity-Verlet integrator [54] and a 0.25 fs timestep. Simulations are run in the canonical (NVT) ensemble, using a Nosé-Hoover style thermostat [55, 56] with a 0.1 ps damping constant. The temperature is fixed to 300 K and the simulation cells have been previously relaxed in the NPT ensemble at this temperature and a pressure of 1 atm using an additional coupling to a barostat [57] with a 1.0 ps damping constant. The diagonal components of the stress tensor were controlled independently so that true hydrostatic conditions were achieved, prior to any elastic constants calculations.

The elastic constants are obtained from stress-strain curves obtained by applying pure tensile or shear strains and the corresponding stresses computed using the virial stress:

$$\boldsymbol{\sigma} = -\frac{1}{\mathcal{V}} \sum_{\alpha \in \mathcal{V}} m^{\alpha} \boldsymbol{v}^{\alpha} \otimes \boldsymbol{v}^{\alpha} - \frac{1}{\mathcal{V}} \sum_{\alpha \in \mathcal{V}} \sum_{\beta \in \mathcal{V}_{\alpha}} \boldsymbol{r}^{\alpha\beta} \otimes \boldsymbol{f}^{\alpha\beta} \quad (2)$$

where $\alpha$ and $\beta$ are indices running on the atoms, $\mathcal{V}$ is the simulation cell volume, $m^{\alpha}$ and $\boldsymbol{v}^{\alpha}$ are the mass and velocity of atom $\alpha$, and $\boldsymbol{r}^{\alpha\beta}$, $\boldsymbol{f}^{\alpha\beta}$ respectively stand for interatomic distance and force vectors and $\otimes$ is the dyadic product. Here, the minimum image convention is used and $\boldsymbol{f}^{\alpha\beta}$ stands for the total force on central atom $\alpha$ due to neighboring atom $\beta$. In addition all velocities are re-centered on the average velocity of the MD simulation cell.

According to Wallace [58] and Sutton [59], any given thermo-elastic process must be associated with either adiabatic (S) or isothermal (T) elastic constants. However, the choice of which type of elastic constant to use depends directly on the rate of elastic deformation. For instance, adiabatic elastic constants are typically measured using ultrasonic pulse experiments, while their isothermal counterparts are usually measured through direct quasi-static mechanical tests at constant temperature. As in a recent investigation on graphite [60], these two distinct sets of elastic constants are computed in this work.

Isothermal (T) elastic constants, which are characterized by low strain rates relative to all elastic relaxation modes of the material, are computed as follows. Starting from the equilibrated microstructure, a series of finite strains are uniformly applied to the simulation cell. The strain range considered in this study is given by $\varepsilon \in [1, 3]$ %, with a 0.1 % increment, for tensile deformations [40]. Compressive strains were not considered to avoid the compression-induced buckling elastic instabilities [61, 38]. For shear strains however, the range considered is $[-1.0, +1.0]$ % with the same increment. Following the application of strain, the simulation cell undergoes equilibration in the NVT ensemble for a duration of 100 ps to allow for stress relaxation via the reorganization of atomic coordinates. The stress tensor is then obtained by averaging stress components over the last 20 ps of the trajectories.

Adiabatic (S) elastic constants, are representative of the elastic response in the limit of instantaneous deformations, without any subsequent relaxation of atomic positions [62, 60]. They are computed as follows. First, the system is equilibrated for 100 ps in the NVT ensemble. Subsequently, a total of 10 independent configurations are selected from the last 20 ps of the NVT simulation, and these configurations are subjected to finite homothetic strains spanning the same values as those employed in the isothermal case, resulting in 10 independent data points for $(\sigma, \varepsilon)$. This process is repeated for different amplitudes and types of strain, yielding 10 stress-strain curves for each deformation type. These curves are then averaged to obtain a single "master" stress-strain curve.

Isothermal $C_{ij}^{T}$ and adiabatic $C_{ij}^{S}$ elastic constants are then determined by performing linear fits of the stress *vs.* strain curves. As in former work [60], $C_{11}$ and $C_{12}$ are averaged from tensile tests performed in the $x$ and $y$ directions, $C_{33}$ is obtained from tensile tests in the $z$ direction, $C_{13}$ is averaged

from tensile tests performed in the $x$, $y$ and $z$ directions (2 independent evaluations along the $z$ axis), $C_{44}$ is averaged from shear tests in the $xz$ and $yz$ planes and $C_{66}$, explicitly calculated from shear tests in the $xy$ plane.

### 2.3. Machine Learning model

The Random Forest Regressor (RFR) [63] is used to derive a relationship between the structural and textural observables $L_a$, $L_c$, OA and the adiabatic/isothermal elastic properties. RFR is a non-parametric machine learning (ML) algorithm used for predicting a specific property given a set of input features commonly called descriptors. It generates a large number of decision trees, each trained on a random subset of descriptors, and combines their predictions to produce a final output. The combination of these predictions from a given number of trees helps reducing overfitting and improves the accuracy of the model. Given a set $\boldsymbol{x}$ of descriptors, the final predicted properties $\boldsymbol{y}$ are averaged over the individual intermediate predictions $\boldsymbol{y_i}$:

$$\boldsymbol{y}(\boldsymbol{x}) = \frac{1}{N_t}\sum_{i=1}^{N_t}\boldsymbol{y_i}(\boldsymbol{x}) \tag{3}$$

with $N_t$ the total number of decision trees.

In this work, the elastic properties are predicted while coherence lengths and orientation angle $L_a$, $L_c$, and OA respectively, play the role of input features. The RFR implementation of the `sklearn` Python library [64] was used with a number of decision trees $N_t = 100$, a tree depth $D_t = 15$ and a minimum number of samples $N^{\text{leaf}}_{\text{samples}} = 5$. The entire dataset was split into two sub-datasets, namely the training (80%) and test (20%) sets, in order to assess the predictive capability of the model and two metrics were used for quantifying the error of the prediction, namely, the Root Mean Squared Error (RMSE) and the coefficient of determination ($R^2$), widely used together in ML techniques.

## 3. Results

### 3.1. Elastic constants within the database

We discuss here the relationship between the material parameters $L_a$, $L_c$ and OA, and the computed elastic constants. Figure 2 shows the entire database of isothermal elastic constants $C^T_{ij}$, displayed as a function of the OA parameter, and color coded according to the $L_a$ parameter (a similar plot for the adiabatic elastic constants is provided in figure S1. It appears clearly that at least four of the six elastic constants are strongly correlated to OA. $C_{11}$ indeed shows a clear decreasing trend with increasing OA, while all the constants involving the transverse direction , $C_{33}$, $C_{13}$ and $C_{44}$, increase with increasing OA, in an almost perfectly linear manner for $C_{13}$ and $C_{44}$. The correlation between OA and the two other constants ($C_{12}$ and $C_{66}$) is weaker, yet as for $C_{11}$, both constants seem to decrease with increasing OA at large OAs ($> 40°$). For these constants, there seems to exist some positive correlation with the coherence lengths, especially $L_a$, at least at low OAs (see figure S2 in the supplementary material). This is also slightly the case for $C_{11}$ and $C_{33}$ which seem to increase slightly with $L_a$ for strongly anisotropic models.

Overall, as shown in figure S1, the same observations apply to adiabatic constants, although in this case, $C_{12}$ shows less variation, and hence, $C_{66}$ – which is a combination of $C_{11}$ and $C_{12}$ – follows the same trend as $C_{11}$. Quantitatively speaking, one observes that adiabatic constants are generally slightly larger than their isothermal counterparts, asides from $C_{12}$ for which adiabatic values are in the lower side of isothermal values. This result is somehow consistent with our former investigation on graphite where it was found that the room temperature isothermal elastic constants were lower than adiabatic ones for all constants but $C_{12}$ and $C_{13}$ [60]. The larger compliance of elastic tensors in the isothermal case stems from the relaxation of atomic positions leading to a decrease in macroscopic stresses.

Despite significant quantitative variations, the hierarchy of elastic constants – $C_{11} > C_{66} > C_{12} > C_{33} \sim C_{13} > C_{44}$ – (figure 2) remains independent of OA in the isothermal case. Although this hierarchy also applies to adiabatic constants at low OAs, some inversions occur at intermediate values, leading to the following order at large OAs: $C_{11} > C_{66} > C_{44} \sim C_{33} > C_{13} > C_{12}$ (figure S1).

Table 1: Comparison of the isothermal ($Cij^T$) elastic constants in GPa of the most ordered (A) and the most disordered (B) models with the values computed for hexagonal graphite in Polewczyk *et al.* [60]. A: OA = 24.8°, $L_c$ = 7.7 nm and $L_a$ = 5.3 nm; B: OA = 109.6°, $L_c$ = 2.1 nm and $L_a$ = 2.1 nm.

| Specimen | $C^T_{11}$ | $C^T_{33}$ | $C^T_{12}$ | $C^T_{13}$ | $C^T_{44}$ | $C^T_{66}$ |
|---|---|---|---|---|---|---|
| Graphite | 943 | 28 | 160 | 6.3 | 0.2 | 389 |
| A | 712 | 11.5 | 83 | 11.3 | 1.0 | 170 |
| B | 289 | 57 | 54 | 48 | 41 | 101 |

It is interesting to describe the properties of the models with highest and lowest degrees of texture and structure in the database, noted A and B, respectively. The isothermal elastic constants of these two models are compared to those computed previously for graphite [60] in Table 1. The longitudinal elastic constants are divided by a factor of $\sim 3$, from graphite to model B, yet the latter retains a high degree of longitudinal stiffness, despite having small domain sizes ($L_a = L_c = 2.1$ nm) and low anisotropy (OA = 109.6°). Conversely, transverse elastic constants significantly increase by factors going from $\sim 2$ for $C^T_{33}$ to $\sim 200$ for $C^T_{44}$ due to the presence of a covalent bond network in the anisotropy direction. Model A, as expected, shows intermediate values between graphite and model B for most constants except $C^T_{33}$. The $C^T_{33}$ value of model A, which is the lowest of the

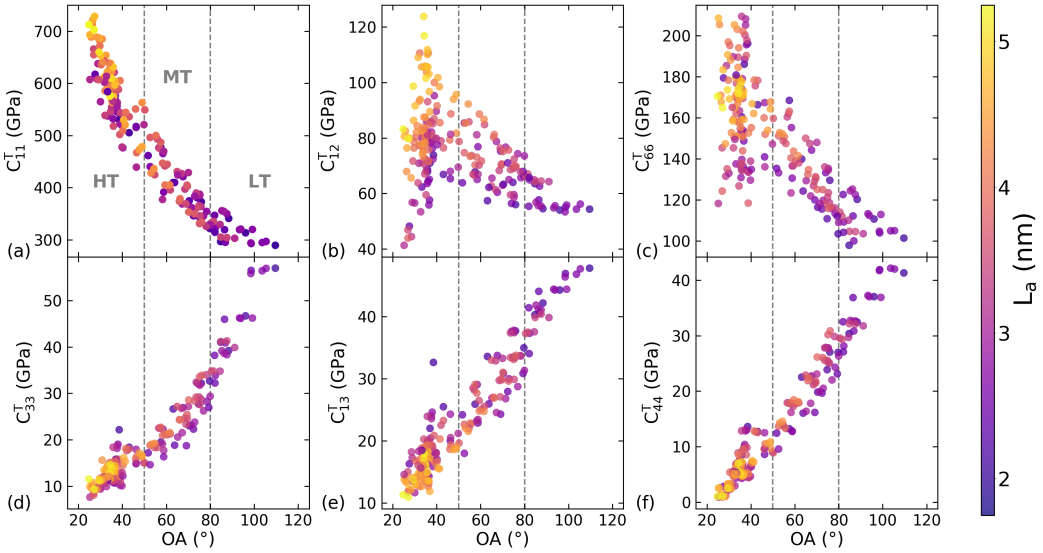


Figure 2: Evolution with OA of the isothermal elastic constants within the database. The data points are color-coded by increasing value of $L_a$ from 2 nm (blue) to 5.5 nm (yellow). Dashed vertical lines indicate the separation between high-texture (HT), medium-texture (MT) and low-texture (LT) domains.

three systems, can be explained by a combination of two phenomena [40]: the decrease in stiffness due to weakened van der Waals interactions, when going from graphite ($d_{002}$ = 0.341 nm) to model A ($d_{002}$ = 0.345 nm), and the increase in stiffness due to an increase in the number, and alignement, of covalent bonds along the anisotropy direction when going from model A to model B. Although some quantitative differences exist, the same observations apply to the adiabatic elastic constants given in table S1.

### *3.2. Supervised-Learning Model*

Figure 3 shows the elastic constants, both adiabatic and isothermal, predicted using the RFR method, using $L_a$, $L_c$ and OA as descriptors (or features), for the entire database, split into training and test (or validation) sets. As can be confirmed with the $R^2$ and RMSE error metrics, given for each type of $C_{ij}$ in tables S2 and S3, RFR predictions are rather accurate, for all constants, despite the very limited set of descriptors. For these predictions using the RFR method, 12 independent models were created to independently predict the 12 adiabatic and isothermal elastic constants from $L_a$, $L_c$ and OA. We carefully checked that doing so was not affecting the calculations of homogenized data such as bulk/shear moduli and universal anisotropy index.

A common practice when using RFR consists in investigating the sensitivity of the prediction to the descriptor set in order to reduce the number of input features. In the present work, the RFR feature importance standardized method was used to extract each features' importance. The importance of the three features in predicting the 12 sets of elastic constants (6 isothermal and 6 adiabatic) is shown in table S6. Considering that features with importance less than 0.05 can be neglected, one observes that three isothermal constants ($C^T_{11}$, $C^T_{33}$ and $C^T_{44}$) and five adiabatic constants ($C^S_{11}$, $C^S_{66}$, $C^S_{33}$, $C^S_{13}$ and $C^S_{44}$) can be accurately predicted using OA as the unique descriptor. The prediction of $C^S_{12}$ requires the full set of features ($L_c$, OA and $L_a$ with relatively balanced weights). Prediction of $C^T_{12}$ requires, by order of importance, $L_a$, then OA and $L_c$. Predictions of $C^T_{66}$ is based on OA, $L_c$ and $L_a$, and $C^T_{13}$ mostly on OA with a little $L_c$.

This feature reduction strategy (feature importance built in the RFR algorithm) was applied to the prediction of both adiabatic and isothermal elastic constants and the equivalent of figure 3 obtained with the reduced feature sets is show in figure S3. The overall quality of the predictions remains close to the one of the full feature model (see also the error metrics $R^2$ and RMSE in tables S4 and S5). We show in figure 4 the evolutions with OA of the eight elastic constants that mostly do not depend on $L_a$ and $L_c$. The comparison of the RFR predictions and MD simulation results shows an excellent agreement.

### *3.3. Elastic anisotropy*

The universal anisotropy index [65], which measures the level of anisotropy of any material from its elastic constants[66], is defined as:

$$A_u = 5\frac{G^V}{G^R} + \frac{K^V}{K^R} - 6 \qquad (4)$$

where $G$ and $K$ indicate estimates of the shear and bulk moduli, respectively, according to the Voigt ($V$ superscript) and Reuss ($R$ superscript) models. The expressions for these terms are given in the supplementary material. The Voigt bound relates to the behavior of a material under an isotropic deformation-imposed process while the Reuss bound is re-

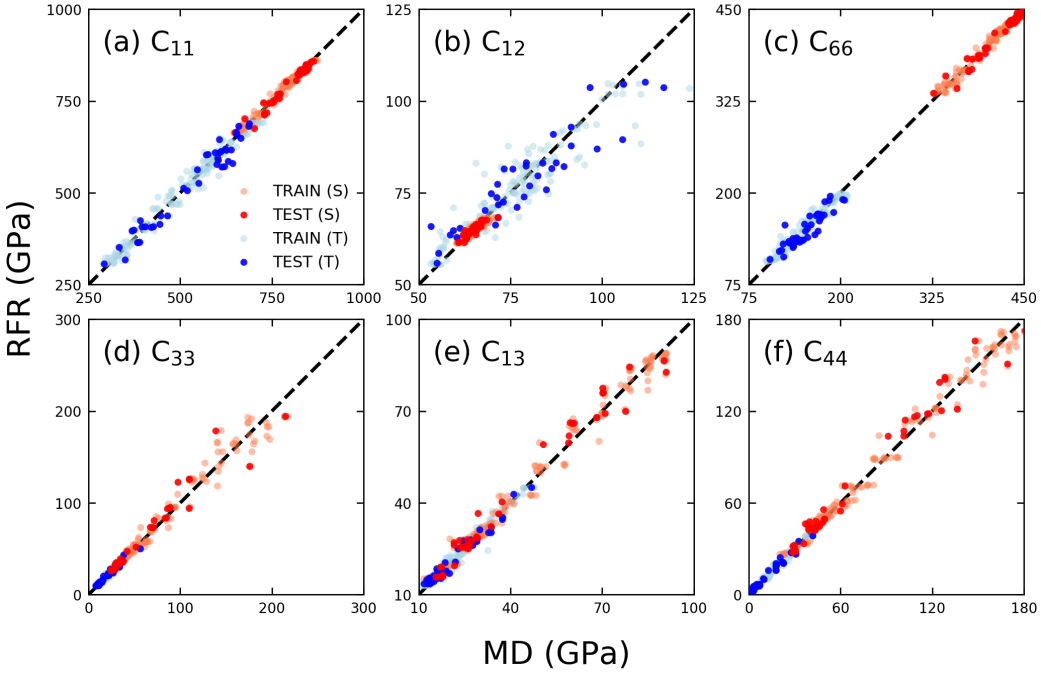


Figure 3: Comparison of RFR predicted and MD computed elastic constants. Training and validation sets are shown with light and dark symbols, respectively; adiabatic (S) and isothermal (T) constants are shown in red and blue, respectively. 12 distinct models were created for prediction of adiabatic and isothermal elastic constants.

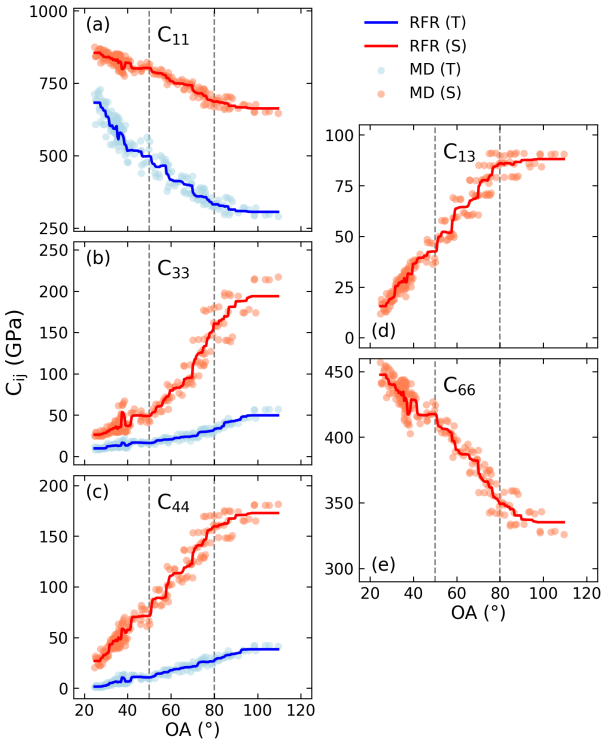


Figure 4: Evolution with OA of eight elastic constants that merely depend on OA. Symbols: MD data; lines RFR model with OA as unique feature; red: adiabatic; blue: isothermal. Dashed vertical lines are as in Fig. 2.

lated to the behavior of a material under an imposed hydrostatic pressure. It is obvious that an isotropic material will behave in the same way under both conditions and hence that $A_u = 0$ for a perfectly isotropic material.

Figure 5 shows the evolution of $A_u$ with OA along the 1 atm isobaric pathway for the isothermal and adiabatic approaches. As expected, the elastic anisotropy, as measured by the $A_u$ parameter, is negatively correlated to OA. Stated otherwise, the elastic anisotropy correlates perfectly well with the textural anisotropy, whatever adiabatic or isothermal elasticity is considered. Under standard conditions of pressure and temperature, the anisotropy indices of the most textured models can reach values of $\sim 35$ and 280 for the adiabatic and isothermal cases, respectively. These very high values place these materials amongst the list of the known materials with the largest elastic anisotropy, despite their low crystallinity [66].

The values presented in figure 5(a,b), are also consistent with the values obtained for graphite – 93 and 2169 for adiabatic and isothermal conditions, respectively [60] – which is the limit at OA = 0 and infinite values of $L_a$ and $L_c$. As shown by the RFR predictions obtained with different values of $L_c$ and $L_a$ (see the colored lines in figure 5), $A_u$ is mostly independent of these coherence lengths when OA $> 50°$. However, for lower OA values, $A_u$ increases with increasing $L_c$ and $L_a$. Interestingly, as shown in figure 5(c), the ratio of isothermal to adiabatic universal anisotropy indices, $A_u^T/A_u^S$, is mostly constant ($\sim 2.5$) for OA values above $\sim 40°$, while this ratio significantly increases when decreas-

ing OA and increasing coherence lengths for lower OA values. Whatever the OA, the elastic anisotropy is larger under isothermal conditions, which indicates that isothermal stress relaxation favors anisotropy.

### *3.4. Elastic properties of actual pyCs*

In Ref. 47, a series of models were identified from the entire database as best matching the properties of a set of actual materials, extensively characterized in previous works [21, 22]. This set comprises a series of high textured pyCs, including an as-prepared rough laminar (RL) pyC, an as prepared regenerative laminar (ReL) pyC and the ReL pyC after heat-treatment at 1300 ($ReL_{1300}$), 1500 ($ReL_{1500}$) and 1700°C ($ReL_{1700}$). For all these materials, the PG-IGAR models were found to be in much better agreement with experimental characterization data than the previously proposed IGAR models [22], especially regarding *c*-axis stacking coherence. Furthermore, the database also contains a model of the as-prepared smooth laminar (SL) pyC, which, to our knowledge, is the first ever atomistic model of a medium textured pyC.

Table 2 gathers the longitudinal ($E_1$) and transverse ($E_3$) Young's moduli, and the three Poisson coefficients ($\nu_{12}$, $\nu_{13}$ and $\nu_{31}$) computed for these models from the isothermal elastic tensors according to :

$$E_1 = \frac{(C_{33}(C_{11}+C_{12})-2C_{13}^2)(C_{11}-C_{12})}{C_{11}C_{33}-C_{13}^2} \quad (5)$$

$$E_3 = \frac{C_{33}(C_{11}+C_{12})-2C_{13}^2}{C_{11}+C_{12}} \quad (6)$$

$$\nu_{13} = \frac{1}{2} - \frac{3}{4}\frac{C_{33}(C_{11}+C_{12})-2C_{13}^2}{(C_{11}+C_{12}+2C_{13}+\frac{C_{33}}{2})(C_{11}+C_{12})} \quad (7)$$

$$\nu_{31} = \frac{E_3\nu_{13}}{E_1} \quad (8)$$

$$\nu_{12} = \frac{C_{11}-E_1-\nu_{13}C_{13}}{C_{12}} \quad (9)$$

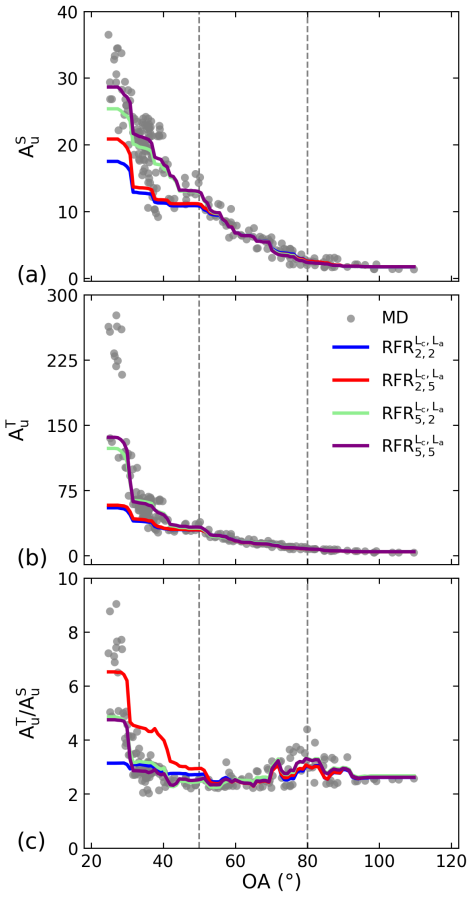


Figure 5: Evolution of (a) $A_u^S$, (b) $A_u^T$ and (c) $A_u^S/A_u^T$ as a function of OA. Symbols: MD data; lines: RFR models with different $\{L_c,L_a\}$ couples in nm. Dashed vertical lines are as in Fig. 2.

Table 2: Isothermal Young's moduli (in GPa), Poisson coefficients and universal anisotropy of pyrocarbon models. Data for hexagonal graphite, by Polewczyk *et al.* [60] are given for comparison.

| Specimen | $E_1$ | $E_3$ | $\nu_{12}$ | $\nu_{13}$ | $\nu_{31}$ | $A_u$ |
|---|---|---|---|---|---|---|
| Graphite | 915 | 28 | 0.16 | 0.48 | 0.01 | 2169 |
| SL | 385 | 22 | 0.43 | 0.47 | 0.03 | 13.9 |
| RL | 663 | 11 | 0.20 | 0.49 | 0.01 | 101 |
| ReL | 530 | 12 | 0.35 | 0.49 | 0.01 | 49.6 |
| $ReL_{1300}$ | 575 | 12 | 0.24 | 0.49 | 0.01 | 49.9 |
| $ReL_{1500}$ | 554 | 12 | 0.25 | 0.49 | 0.01 | 64.5 |
| $ReL_{1700}$ | 683 | 9 | 0.18 | 0.49 | 0.01 | 263 |

We observe that the SL pyC model has the lowest value for $E_1$ (385 GPa), the largest value for $E_3$ (22 GPa) aside from graphite, and the largest Poisson coefficients $\nu_{12}$ and $\nu_{31}$, compared to the other pyCs. Amongst the high textured pyC models, we observe that $E_1$ and $A_u$, also given in table 2, increase with heat treatment temperature for the ReL pyC, while, conversely, $E_3$ and $\nu_{12}$ decrease. As for the structural parameters (see Ref. 47), the elastic properties of the ReL pyCs become similar to those of the as-prepared RL pyC, after heat treatment of the former to values between 1500 and 1700°C.

The results presented here in table 2 are relatively similar to those obtained with the IGAR models for the HT pyCs [40], especially for $E_1$ values. For the other constants, some quantitative differences exist, at least in part due to the use of different interatomic potentials for computing the elastic tensors. Yet, for instance, the decrease in $E_3$ with increasing heat treatment temperature for the ReL pyC is consistent in the two sets of data. However, as in Ref. 40, the values obtained for $E_1$ are not consistent with the experimental results of Sauder *et al.* [35], who reported values of 54, 115, 205 and 245 GPa for the SL, RL, ReL and the ReL pyC heat treated at 1600°C, respectively. Although the pyC matrices investigated by Sauder *et al.* may differ slightly from those characterized by Weisbecker *et al.* [21] and Farbos *et al.*

[22], from which the data were later used to identify the pyC models, the much lower moduli measured by Sauder *et al.* [35] indicate that something is lacking in the current models. This cannot be the absence of hydrogen as Farbos *et al.* have shown that accounting for hydrogen would, at best, lead to a 12 % decrease of $E_1$. Also, it is worth noting that while the results by Sauder *et al.* agree in finding that the SL pyC has the lowest $E_1$, they observed that the ReL pyC has a modulus twice as large as the SL pyC, which, as mentioned in the introduction, seems counter-intuitive with respect to the characterization data. All of this suggests that tensile moduli of the pyC matrices are dominated by structural/textural features at a larger scale. It is indeed well-known that pyC matrices show texture effects at much larger scales. This is particularly well illustrated in the case of ReL in the dark-field or Lattice-fringe TEM micrographs of Bourrat et al. [67] and of various pyrocarbons in the TEM micrographs of Ozcan et al. [68]

## 4. Conclusion

In this report, we have used MD simulations to compute the elastic tensors of a large database of dense anisotropic carbons, from high to low texture, under both isothermal and adiabatic conditions. These properties were compared with computed nanostructural ($L_c$, $L_a$) and nanotextural (OA) parameters, allowing to disentangle for the first time the respective effects of texture and structure, for this class of materials. Although both approaches lead to very different ranges of values for the elastic constants due to the lack of relaxation of atomic positions in the adiabatic approach, we show that, in both cases, the texture parameter OA has, by far, the strongest influence on the elastic constants. A random forest regressor algorithm was trained on the database and it was shown that all the elastic constants can be accurately predicted from OA, $L_c$ and $L_a$. A feature reduction process has allowed to show that 5 adiabatic and 3 isothermal constants can be accurately predicted using OA as sole descriptor. Data regarding the entire database (structural and textural parameters, isothermal and adiabatic constants) is provided as supporting material. The RFR model, that allows for the first time the quantitative prediction of all elastic constants from OA, $L_a$ and $L_c$, is available online at `https://web.ism.u-bordeaux.fr/rfr`.

Calculation of the universal anisotropy ($A_u$) index has shown that elastic anisotropy increases with textural anisotropy. Also it was shown that $A_u$ is larger for isothermal tensors with respect to adiabatic tensors, with a factor of $\sim 2.5$ for medium to low texture carbons (OA $> 50°$), a factor that significantly increases with decreasing OA at lower OA values (i.e. for HT pyCs). This indicates that high texture carbons exhibit very different elastic behaviors depending on the loading conditions, as for graphite.

Finally, the isothermal Young moduli and Poisson coefficients of six models of actual pyCs were described and the longitudinal moduli compared to tensile test results from Sauder *et al.* [35]. While the elasticity of the nanoscale models identified in this work seems reasonable, the obtained longitudinal moduli are significantly larger than the experimental data. This suggests that the latter may result from textural patterns at a larger scale, possibly at the scale of the growth cones in pyC deposits. Future work will aim at builing a meso-scale model of the matrices, informed by orientation data derived from characterization techniques operating at the $\mu$m scale like polarized light optical microscopy, and in which the model presented in this work will provide the local elasticity tensors.

## CRediT

**Franck Polewczyk**: Methodology, Software, Formal analysis, Investigation, Data curation, Writing – original draft. **Jean-Marc Leyssale**: Conceptualization, Methodology, Formal analysis, Resources, Data curation, Validation, Writing – original **Philippe Aurel**: Software, Writing – review & editing. **Nicolas Pineau**: Conceptualization, Formal analysis, Resources, Validation, Writing – review & editing. **Christophe Denoual**: Conceptualization, Formal analysis, Resources, Validation, Writing – review & editing. **Gerard L. Vignoles**: Conceptualization, Formal analysis, Resources, Validation, Writing – review & editing. **Paul Lafourcade**: Conceptualization, Methodology, Software, Formal analysis, Resources, Data curation, Writing – original draft.

## Declaration of competing interest

The authors declare that they have no known competing financial interests or personal relationships that could have appeared to influence the work reported in this paper.

## Acknowledgments

Financial support from the French Ministry of Defence - Defence Innovation Agency is gratefully acknowledged by FP. Atomistic simulations were performed using the computational resources of the CEA/DAM.

## References

[1] I. L. Shabalin, Ultra-High Temperature Materials I, Springer, Dordrecht, 2014. doi:10.1007/978-94-007-7587-9.

[2] F. Vuković, J.-M. Leyssale, P. Aurel, N. A. Marks, Evolution of threshold displacement energy in irradiated graphite, Phys. Rev. Appl. 10 (2018) 064040. doi:10.1103/PhysRevApplied.10.064040.

[3] G. Savage, Carbon-carbon composites, Chapman and Hall, London, 1993. doi:10.1007/978-94-011-1586-5.

[4] E. Fitzer, L. M. Manocha, Carbon reinforcements and C/C composites, 1st ed., Berlin: Springer, 1998. doi:10.1007/978-3-642-58745-0.

[5] H. Hatta, R. Weiß, P. David, Carbon/carbons and their industrial applications, in: N. P. Bansal, J. Lamon (Eds.), Ceramic Matrix Composites : Materials, Modeling and Technology, John Wiley & Sons, Ltd, 2014, Ch. 5, pp. 85–146. doi:10.1002/9781118832998.ch5.

[6] J. Choury, Carbon-carbon materials for nozzles of solid propellant rocket motors, in: Proceedings of the $12^{th}$ Propulsion Conference, 1976. doi:10.2514/6.1976-609.

[7] G. L. Vignoles, J. Lachaud, Y. Aspa, Environmental effects: Ablation of C/C materials – surface dynamics and effective reactivity, in: N. P. Bansal, J. Lamon (Eds.), Ceramic Matrix Composites: Materials, Modeling and Technology, Wiley & American Ceramic Society, 2014, Ch. 12, pp. 353–384. doi:10.1002/9781118832998.ch12.

[8] S. Awasthi, J. L. Wood, Carbon/Carbon Composite Materials for Aircraft Brakes, John Wiley & Sons, Ltd, 1988, Ch. 4, pp. 553–559. doi:10.1002/9780470310496.ch4.

[9] A. Oberlin, Pyrocarbons, Carbon 40 (2002) 7–24. doi:10.1016/S0008-6223(01)00138-5.

[10] G. L. Vignoles, Chemical vapor deposition/infiltration processes for ceramic composites, in: P. Boisse (Ed.), Advances in Composites Manufacturing and Process Design, Elsevier Woodhead Scientific, 2016, Ch. 8, pp. 147–176. doi:10.1016/B978-1-78242-307-2.00008-7.

[11] P. Delhaès, Chemical vapor deposition and infiltration processes of carbon materials, Carbon 40 (5) (2002) 641–657. doi:https://doi.org/10.1016/S0008-6223(01)00195-6.

[12] H. Duan, Z. Zhang, L. Li, W. Li, Effect of pyrocarbon interphase texture and thickness on tensile damage and fracture in T-700™ carbon fiber–reinforced silicon carbide minicomposites, J. Am. Ceram. Soc. 105 (3) (2022) 2171–2181. doi:10.1111/jace.18193.

[13] J. Xu, L. Guo, H. Wang, K. Li, T. Wang, W. Li, Mechanical property and toughening mechanism of 2.5D C/C-SiC composites with high textured pyrocarbon interface, Ceram. Int. 47 (20) (2021) 29183–29190. doi:10.1016/j.ceramint.2021.07.081.

[14] B. Heidenreich, C/SiC and C/C-SiC composites, in: N. P. Bansal, J. Lamon (Eds.), Ceramic Matrix Composites: Materials, Modeling and Technology, John Wiley & Sons, Ltd, 2014, Ch. 6, pp. 147–216. doi:10.1002/9781118832998.ch6.

[15] R. R. Naslain, The design of the fibre-matrix interfacial zone in ceramic matrix composites, Compos. Part A 29 (9) (1998) 1145–1155. doi:10.1016/S1359-835X(97)00128-0.

[16] R. Naslain, Design, preparation and properties of non-oxide CMCs for application in engines and nuclear reactors: an overview, Compos. Sci. Technol. 64 (2004) 155–170. doi:10.1016/S0266-3538(03)00230-6.

[17] E. Buet, J. Braun, C. Sauder, Influence of texture and thickness of pyrocarbon coatings as interphase on the mechanical behavior of specific 2.5D SiC/SiC composites reinforced with Hi-Nicalon S fibers, Coatings 12 (5) (2022). doi:10.3390/coatings12050573.

[18] A. Koster, H. Matzner, D. Nicholsi, PBMR design for the future, Nucl. Eng. Des. 222 (2) (2003) 231–245, hTR-2002 1st international topical meeting on High Temperature reactor technology. doi:https://doi.org/10.1016/S0029-5493(03)00029-3.

[19] Y. Ohzawa, M. Mitani, J. Li, T. Nakajima, Structures and electrochemical properties of pyrolytic carbon films infiltrated from gas phase into electro-conductive substrates derived from wood, Mater. Sci. Eng. B Solid State Mater. Adv. Technol. 113 (1) (2004) 91–98. doi:10.1016/j.mseb.2004.07.006.

[20] J. Bokros, Carbon biomedical devices, Carbon 15 (6) (1977) 353–371. doi:https://doi.org/10.1016/0008-6223(77)90324-4.

[21] P. Weisbecker, J.-M. Leyssale, H. E. Fischer, V. Honkimäki, M. Lalanne, G. L. Vignoles, Microstructure of pyrocarbons from pair distribution function analysis using neutron diffraction, Carbon 50 (2012) 1563–1573. doi:https://doi.org/10.1016/j.carbon.2011.11.035.

[22] B. Farbos, P. Weisbecker, H. Fischer, J.-P. Da Costa, M. Lalanne, G. Chollon, C. Germain, G. Vignoles, J.-M. Leyssale, Nanoscale structure and texture of highly anisotropic pyrocarbons revisited with transmission electron microscopy, image processing, neutron diffraction and atomistic modeling, Carbon 80 (2014) 472–489. doi:https://doi.org/10.1016/j.carbon.2014.08.087.

[23] T. Wu, C. Lu, T. Sun, Y. Li, S. Yuan, D. Li, G. Wang, X. Ren, New discovery on the relationship between microstructure and tensile strength of pan-based carbon fibers, Microporous Mesoporous Mater. 330 (2022) 111584. doi:https://doi.org/10.1016/j.micromeso.2021.111584.

[24] X. Bourrat, B. Trouvat, G. Limousin, G. Vignoles, F. Doux, Pyrocarbon anisotropy as measured by electron diffraction and polarized light, J. Mater. Res. 15 (1) (2000) 92–101. doi:https://doi.org/10.1557/JMR.2000.0017.

[25] B. Reznik, K. Hüttinger, On the terminology for pyrolytic carbon, Carbon 40 (4) (2002) 621–624. doi:https://doi.org/10.1016/S0008-6223(01)00282-2.

[26] M. Folomeshkin, Y. Pisarevsky, P. Prosekov, Y. A. Volkovsky, A. S. Kumskova, Y. V. Grigoriev, E. A. Ligacheva, A. V. Targonskii, A. E. Blagov, M. V. Kovalchuk, X-ray diffraction analysis and electron microscopy of the carbon fiber structure, Crystallogr. Rep. 64 (1) (2019) 1–5. doi:https://doi.org/10.1134/S1063774519010085.

[27] R. E. Smith, Ultrasonic elastic constants of carbon fibers and their composites, J. Appl. Phys. 43 (1972) 2555–2561. doi:https://doi.org/10.1063/1.1661559.

[28] T. Csanádi, D. Németh, C. Zhang, J. Dusza, Nanoindentation derived elastic constants of carbon fibres and their nanostructural based predictions, Carbon 119 (2017) 314–325. doi:https://doi.org/10.1016/j.carbon.2017.04.048.

[29] F. Tanaka, T. Ishikawa, M. Tane, A comprehensive review of the elastic constants of carbon fibers: implications for design and manufacturing of high-performance composite materials, Adv. Composite Mater. 0 (0) (2023) 1–21. doi:10.1080/09243046.2023.2245210.

[30] E. P. Papadakis, H. Bernstein, Elastic moduli of pyrolytic graphite, J. Acoust. Soc. Am. 35 (4) (1963) 521–524. doi:10.1121/1.1918521.

[31] J.-M. Gebert, B. Reznik, R. Piat, B. Viering, K. Weidenmann, A. Wanner, O. Deutschmann, Elastic constants of high-texture pyrolytic carbon measured by ultrasound phase spectroscopy, Carbon 48 (12) (2010) 3647–3650. doi:10.1016/j.carbon.2010.06.002.

[32] O. L. Blakslee, D. G. Proctor, E. J. Seldin, G. B. Spence, T. Weng, Elastic constants of compression-annealed pyrolytic graphite, J. Appl. Phys. 41 (8) (1970) 3373–3382. doi:10.1063/1.1659428.

[33] T. Böhlke, T.-A. Langhoff, S. Lin, T. Gross, Homogenization of the elastic properties of pyrolytic carbon based on an image processing technique, ZAMM - J. Appl. Math. Mech. / Zeit. Angew. Math. Mech. 93 (5) (2013) 313–328. doi:https://doi.org/10.1002/zamm.201100180.

[34] S. Lin, T.-A. Langhoff, T. Böhlke, Micromechanical estimate of the elastic properties of the coherent domains in pyrolytic carbon, Arch. Appl. Mech. 84 (2014) 133–148. doi:10.1007/s00419-013-0789-7.

[35] C. Sauder, J. Lamon, R. Pailler, The tensile properties of carbon matrices at temperatures up to 2200°c, Carbon 43 (10) (2005) 2054–2065. doi:10.1016/j.carbon.2005.03.020.

[36] P. Diss, J. Lamon, L. Carpentier, J. Loubet, P. Kapsa, Sharp indentation behavior of carbon/carbon composites and varieties of carbon, Carbon 40 (14) (2002) 2567–2579. doi:10.1016/S0008-6223(02)00169-0.

[37] M. Guellali, R. Oberacker, M. Hoffmann, Influence of heat treatment on microstructure and properties of highly textured pyrocarbons deposited during cvd at about 1100°c and above 2000°c, Compos. Sci. Technol. 68 (5) (2008) 1122–1130. doi:10.1016/j.compscitech.2007.07.019.

[38] J.-M. Leyssale, G. Couégnat, S. Jouannigot, G. L. Vignoles,

Mechanisms of elastic softening in highly anisotropic carbons under in-plane compression/indentation, Carbon 197 (2022) 425–434. doi:https://doi.org/10.1016/j.carbon.2022.06.063.

[39] T. Gross, N. Timoshchuk, I. Tsukrov, R. Piat, B. Reznik, On the ability of nanoindentation to measure anisotropic elastic constants of pyrolytic carbon, Z. angew. Math. Mech. 93 (5) (2013) 301–312. doi:10.1002/zamm.201100128.

[40] B. Farbos, J.-P. Da Costa, G. Vignoles, J.-M. Leyssale, Nanoscale elasticity of highly anisotropic pyrocarbons, Carbon 94 (2015) 285–294. doi:10.1016/j.carbon.2015.06.060.

[41] H. Zhang, E. López-Honorato, P. Xiao, Fluidized bed chemical vapor deposition of pyrolytic carbon-iii. relationship between microstructure and mechanical properties, Carbon 91 (2015) 346–357. doi:10.1016/j.carbon.2015.05.009.

[42] I. Y. Stein, A. J. Constable, N. Morales-Medina, C. V. Sackier, M. E. Devoe, H. M. Vincent, B. L. Wardle, Structure-mechanical property relations of non-graphitizing pyrolytic carbon synthesized at low temperatures, Carbon 117 (2017) 411–420. doi:10.1016/j.carbon.2017.03.001.

[43] R. Piat, B. Reznik, E. Schnack, D. Gerthsen, Modeling the effect of microstructure on the elastic properties of pyrolytic carbon, Carbon 41 (9) (2003) 1858–1862. doi:10.1016/S0008-6223(03)00142-8.

[44] J. Kabel, T. E. Edwards, A. Sharma, J. Michler, P. Hosemann, Direct observation of the elasticity-texture relationship in pyrolytic carbon via in situ micropillar compression and digital image correlation, Carbon 182 (2021) 571–584. doi:10.1016/j.carbon.2021.06.045.

[45] J.-M. Leyssale, J.-P. Da Costa, C. Germain, P. Weisbecker, G. L. Vignoles, An image-guided atomistic reconstruction of pyrolytic carbons, Appl. Phys. Lett. 95 (2009) 231912. doi:10.1063/1.3272949.

[46] J.-M. Leyssale, J.-P. Da Costa, C. Germain, P. Weisbecker, G. L. Vignoles, Structural features of pyrocarbon atomistic models constructed from transmission electron microscopy images, Carbon 50 (12) (2012) 4388–4400. doi:https://doi.org/10.1016/j.carbon.2012.05.015.

[47] F. Polewczyk, P. Lafourcade, J.-P. D. Costa, G. Vignoles, J.-M. Leyssale, Polygranular image guided atomistic reconstruction: A parametric model of pyrocarbon nanostructure, Carbon 212 (2023) 118109. doi:10.1016/j.carbon.2023.118109.

[48] D. W. Brenner, O. A. Shenderova, J. A. Harrison, S. J. Stuart, B. Ni, S. B. Sinnott, A second-generation reactive empirical bond order (REBO) potential energy expression for hydrocarbons, J. Phys.: Condens. Matt. 14 (4) (2002) 783–802. doi:10.1088/0953-8984/14/4/312.

[49] B. Farbos, H. Freeman, T. Hardcastle, J.-P. Da Costa, R. Brydson, A. J. Scott, P. Weisbecker, C. Germain, G. L. Vignoles, J.-M. Leyssale, A time-dependent atomistic reconstruction of severe irradiation damage and associated property changes in nuclear graphite, Carbon 120 (2017) 111–120. doi:https://doi.org/10.1016/j.carbon.2017.05.009.

[50] J. Barthel, Dr. Probe: A software for high-resolution STEM image simulation, Ultramicroscopy 193 (2018) 1–11. doi:https://doi.org/10.1016/j.ultramic.2018.06.003.

[51] L. Soulard, Molecular Dynamics Study of the Micro-spallation, Eur. Phys. J. D 50 (3) (2008) 241–251. doi:10.1140/epjd/e2008-00212-2.

[52] J. H. Los, L. M. Ghiringhelli, E. J. Meijer, A. Fasolino, Improved long-range reactive bond-order potential for carbon. i. construction, Phys. Rev. B 72 (2005) 214102. doi:10.1103/PhysRevB.72.214102.

[53] J. H. Los, N. Pineau, G. Chevrot, G. Vignoles, J.-M. Leyssale, Formation of multiwall fullerenes from nanodiamonds studied by atomistic simulations, Phys. Rev. B 80 (2009) 155420. doi:10.1103/PhysRevB.80.155420.

[54] L. Verlet, Computer" experiments" on classical fluids. ii. equilibrium correlation functions, Phys. Rev. 165 (1) (1968) 201. doi:10.1103/PhysRev.165.201.

[55] S. Nosé, A unified formulation of the constant temperature molecular dynamics methods, J. Chem. Phys. 81 (1) (1984) 511–519. doi:10.1063/1.447334.

[56] W. G. Hoover, Canonical dynamics: Equilibrium phase-space distributions, Phys. Rev. A 31 (3) (1985) 1695–1697. doi:10.1103/PhysRevA.31.1695.

[57] G. J. Martyna, D. J. Tobias, M. L. Klein, Constant pressure molecular dynamics algorithms, J. Chem. Phys. 101 (5) (1994) 4177–4189. doi:10.1063/1.467468.

[58] D. Wallace, Thermodynamics of Crystals, Wiley, 1972.

[59] A. Sutton, Physics of Elasticity and Crystal Defects, Oxford Series on Materials Modelling, OUP Oxford, 2020. doi:10.1093/oso/9780198860785.001.0001.

[60] F. Polewczyk, J.-M. Leyssale, P. Lafourcade, Temperature-dependent elasticity of single crystalline graphite, Comput. Mater. Sci. 220 (2023) 112045. doi:10.1016/j.commatsci.2023.112045.

[61] P. Lafourcade, C. Denoual, J.-B. Maillet, Elastic instability in graphite single crystal under dynamic triaxial compression: Effect of strain-rate on the resulting microstructure, J. Appl. Phys. 128 (4) (2020) 045101. doi:10.1063/5.0009724.

[62] P. Lafourcade, C. Denoual, J.-B. Maillet, Dislocation core structure at finite temperature inferred by molecular dynamics simulations for 1,3,5-triamino-2,4,6-trinitrobenzene single crystal, J. Phys. Chem. C 121 (13) (2017) 7442–7449. doi:10.1021/acs.jpcc.6b11576.

[63] L. Breiman, Random forests, Machine Learning 45 (2001) 5–32. doi:10.1023/A:1010933404324.

[64] F. Pedregosa, G. Varoquaux, A. Gramfort, V. Michel, B. Thirion, O. Grisel, M. Blondel, P. Prettenhofer, R. Weiss, V. Dubourg, J. Vanderplas, A. Passos, D. Cournapeau, M. Brucher, M. Perrot, Édouard Duchesnay, Scikit-learn: Machine learning in Python, J. Mach. Learn. Res. 12 (85) (2011) 2825–2830. doi:10.5555/1953048.2078195.

[65] S. I. Ranganathan, M. Ostoja-Starzewski, Universal elastic anisotropy index, Phys. Rev. Lett. 101 (2008) 055504. doi:10.1103/PhysRevLett.101.055504.

[66] C. M. Kube, Elastic anisotropy of crystals, AIP Adv. 6 (9) (2016) 095209. doi:10.1063/1.4962996.

[67] X. Bourrat, A. Fillion, R. Naslain, G. Chollon, M. Brendlé, Regenerative laminar pyrocarbon, Carbon 40 (15) (2002) 2931–2945. doi:https://doi.org/10.1016/S0008-6223(02)00230-0.
URL https://www.sciencedirect.com/science/article/pii/S0008622302002300

[68] S. Ozcan, J. Tezcan, P. Filip, Microstructure and elastic properties of individual components of c/c composites, Carbon 47 (15) (2009) 3403–3414. doi:https://doi.org/10.1016/j.carbon.2009.07.057.
URL https://www.sciencedirect.com/science/article/pii/S0008622309004692